Metasurface-Assisted Quantum Ghost Discrimination of Polarization Objects

Andres Vega,[1,*] Thomas Pertsch,[1,2] Frank Setzpfandt,[1] and Andrey A. Sukhorukov[3,4,†]

[1] *Institute of Applied Physics, Abbe Center of Photonics, Friedrich Schiller University Jena, Albert-Einstein-Str. 15, Jena 07745, Germany*

[2] *Fraunhofer Institute for Applied Optics and Precision Engineering IOF, Albert-Einstein-Str. 7, Jena 07745, Germany*

[3] *Research School of Physics, Australian National University, Canberra ACT 2601, Australia*

[4] *ARC Centre of Excellence for Transformative Meta-Optical Systems (TMOS), Australia*

(Received 6 July 2021; revised 22 November 2021; accepted 30 November 2021; published 13 December 2021)

We develop a concept of metasurface-assisted ghost imaging for nonlocal discrimination between a set of polarization objects. The specially designed metasurfaces are incorporated in the imaging system to perform parallel state transformations in general elliptical bases of quantum-entangled or classically correlated photons. Then, only four or fewer correlation measurements between multiple metasurface outputs and a simple polarization-insensitive bucket detector after the object can allow for the identification of fully or partially transparent polarization elements and their arbitrary orientation angles. The approach can find applications for real-time and low-light imaging across diverse spectral regions in dynamic environments.

DOI: 10.1103/PhysRevApplied.16.064032

I. INTRODUCTION

Optical imaging of polarization properties provides a rich amount of otherwise hidden information, with applications spanning from microscopy [1] to monitoring from satellites [2]. While manipulation and measurement of polarization is conventionally performed using bulk optical elements [3], nanostructured metasurfaces allow the most flexible in-parallel polarization transformations for single-shot measurements [4], real-time imaging with a camera [5], quantum light manipulation, and characterization [6–10].

Fundamental and applied interest in polarization detection at low-light illumination and across broad spectral regions, for example for bio-sensing, motivate the development of polarization ghost imaging [11]. Such schemes draw on the underlying principle originally developed for spatial ghost imaging, where the photons passing through an object are registered with a simple bucket detector [12,13], while their quantum or classically correlated pairs can be conveniently imaged at a different wavelength selected for efficient high-resolution detection [14–16]. The object is characterized through multiple coincidence or correlation measurements [17] that can deliver a better signal-to-noise ratio compared to classical imaging systems, and also enable imaging with a very low number of photons [18,19]. However, there remains a fundamental limitation of traditional ghost polarimetry approaches due to a need for multiple reconfigurable elements such as rotating waveplates [20–27]. Yet, the unique capabilities of polarization control with metasurfaces towards potential single-shot ghost imaging configurations remains largely untapped, so far limited to the incorporation of metasurfaces for hologram generation [28].

In this work we present a concept of metasurface-assisted polarization ghost imaging. We show that by placing specially designed metasurfaces before the polarization-insensitive photon detectors, one can perform discrimination between fully or partially transparent polarization-sensitive objects within a defined set. Furthermore, in our scheme the orientation angle of each object can be simultaneously recognized from only four or fewer parallel correlation measurements. This can facilitate real-time identification of different samples for potential applications including microscopy, whereas full ghost polarimetry requires at least eight measurements with multiple time-consuming reconfigurations to determine all elements of a general Jones matrix form [25]. We also note that only discrimination of nonbirefringent objects with different transversely varying transmission profiles and fixed orientations was realized previously [29].

Furthermore, we demonstrate the role of the degree of entanglement in ghost polarimetry. Entanglement is the most prominent feature in quantum mechanics and has become the cornerstone of rising technologies such

*andres.vega@uni-jena.de
†andrey.sukhorukov@anu.edu.au

as quantum computing [30,31], communication [32], and metrology [33,34]. This curious property enables unique nonlocal measurements since information about the properties of one particle can be obtained by performing a measurement on its entangled partner. Importantly, the correlations between quantum-entangled photons can provide additional information on the phase differences between various polarization components, which might not be detected with classical light.

The paper is organized as following. In Sec. II, we present the concept and develop a theory of the metasurface-assisted scheme for quantum ghost discrimination of polarization objects. In the following Sec. III, we discuss the advantage of stronger two-photon entanglement for object identification. Finally, in Sec. IV we summarize the results and provide a concluding discussion.

II. QUANTUM GHOST POLARIMETRY

Our proposed measurement scheme is depicted in Fig. 1. We consider a source producing a pair of probe and reference photons, which are entangled in the polarization state. Then, according to the principle of ghost imaging, only the probe photon passes through the object characterized by a polarization Jones matrix Ω. We also consider a possible rotation of the object by an angle θ, such that $\Omega(\theta) = R(\theta)\Omega R(-\theta)$, where $R(\theta)$ is a rotation matrix in the counterclockwise direction. The probe photon then passes through a metasurface and is registered by a polarization-insensitive click detector. The paired reference photon does not interact with the object. We place a tailored metasurface in its path, which splits the output between several polarization-insensitive detectors depending on the reference polarization state. We show in the following that by specially designing the metasurfaces, the coincidence measurements between the probe and reference at different detectors enables discrimination between polarization objects, and simultaneous identification of an arbitrary object orientation angle.

The polarization state of the photon-pairs can be defined by the density matrix

$$\rho_{\text{in}} = \tfrac{1}{2}(|H_P H_R\rangle\langle H_P H_R| + |V_P V_R\rangle\langle V_P V_R|) + q\,\tfrac{1}{2}(|H_P H_R\rangle\langle V_P V_R| + |V_P V_R\rangle\langle H_P H_R|), \quad (1)$$

where q is equal to the concurrence [35] and represents the degree of entanglement with $0 \le q \le 1$, from the strongest classical correlation $q = 0$ to perfect entanglement $q = 1$, with the Bell parameter [36] value $S = \sqrt{2}(1+q)$. Throughout this manuscript, horizontal and vertical polarization are denoted H and V, respectively.

The transformation of the probe photon polarization is defined by the Jones polarization transfer matrices of the object $\Omega(\theta)$ and the metasurface M_P. For the reference photon, there are several outputs after the metasurface with the Jones matrices $M_{R,n}$ for the different diffraction orders n.

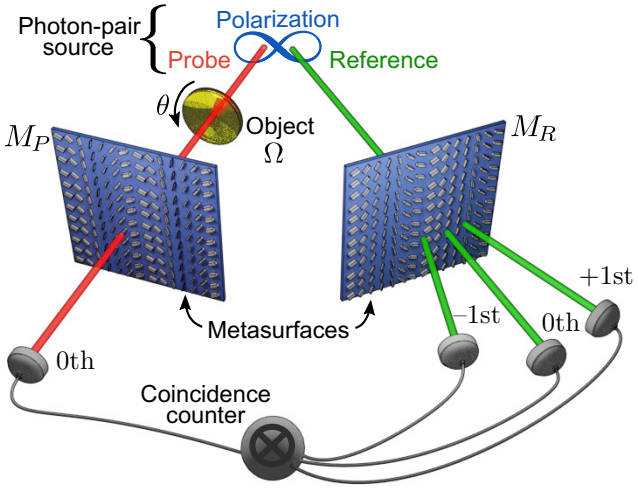

FIG. 1. Sketch of the setup. Polarization transformations by metasurfaces in front of polarization-insensitive detectors enable discrimination of polarization objects Ω and their orientation angles θ through the coincidence measurements.

A. Probe-arm metasurface enabling polarization object discrimination

After detection of the probe photon, the reduced state of the reference photon before the metasurface M_R is determined according to the principle of remote state preparation [37] as $\rho'_R = \text{tr}_P[(T_P \otimes \mathbb{1})\rho_{\text{in}}(T_P \otimes \mathbb{1})^\dagger]$, where $\text{tr}_P(\cdot)$ is the partial trace over the probe photon and $T_P = M_P\Omega(\theta)$. The normalized reduced state is then $\rho_R = \rho'_R/\text{tr}(\rho'_R)$. The expectation values of the coincidence counts between the probe and reference detectors are $\Gamma_n = \text{tr}[(M_{R,n})\rho_R(M_{R,n})^\dagger]$. We show in the following that the metasurfaces can be optimized to realize such M_P and $M_{R,n}$, so that every reduced state ρ_R produces a distinctive pattern formed by a collection of coincidence measurements, thereby allowing discrimination between the objects.

We determine the optimal choice of the M_P metasurface transformation for the probe photon by geometrically representing the reduced state of the reference photon ρ_R in the Poincaré sphere [38], where each ρ_R is described by a vector $\mathbf{p} = [p_H, p_D, p_C]$. Here, p_H corresponds to the degree of horizontal or vertical polarization, p_D to the diagonal $[(|H\rangle + |V\rangle)/\sqrt{2}]$ or antidiagonal linear polarization at $\pm 45^\circ$, and p_C to the right $[(|H\rangle - i|V\rangle)/\sqrt{2}]$ or left circular polarization. Hence, p_H, p_D, p_C correspond to the Stokes parameters s_1, s_2, s_3 [39], respectively. The Poincaré vector is found using the Pauli matrices X, Y, Z with $\mathbf{p} = [\text{tr}(\rho_R Z), \text{tr}(\rho_R X), -\text{tr}(\rho_R Y)]$. If the total transformation in the probe arm, comprising the object Ω and

metasurface M_P, is written in the basis of the photon-pair source as $T_P = \sum T_{kl}|k\rangle\langle l|$ with $k, l \in \{H, V\}$, then

$$p_H = \|T_P\|_F^{-2}(|T_{HH}|^2 + |T_{VH}|^2 - |T_{VV}|^2 - |T_{HV}|^2), \quad (2)$$

$$p_D = 2q\|T_P\|_F^{-2}\mathrm{Re}(T_{HH}T_{HV}^* + T_{VH}T_{VV}^*), \quad (3)$$

$$p_C = 2q\|T_P\|_F^{-2}\mathrm{Im}(T_{HH}T_{HV}^* + T_{VH}T_{VV}^*), \quad (4)$$

where $\|\cdot\|_F$ is the Frobenius norm. Since we require that each object produces a different reduced state, each ρ_R must occupy a unique position on or inside the Poincaré sphere.

We reveal an important relation between the components of the Poincaré vector as $p_H^2 + (p_D^2 + p_C^2)/q^2 = 1 - 4|\det(T_P)|^2/\|T_P\|_F^4$, where $\det(\cdot)$ is the determinant, $|\det(T_P)| = \prod_l \sigma_{lP}$, and $\|T_P\|_F^2 = \sum_l \sigma_{lP}^2$, leading to

$$p_H^2 + \frac{p_D^2 + p_C^2}{q^2} = \eta^2 = \left(\frac{\sigma_{1P}^2 - \sigma_{2P}^2}{\sigma_{1P}^2 + \sigma_{2P}^2}\right)^2, \quad (5)$$

where σ_{1P} and σ_{2P} are the singular values of the transformation T_P. Equation (5) indicates that the reduced state of the reference photon ρ_R obtained from the family of transformations T_P that have the same η will lie on an ellipsoid of revolution of long axis η and short axis $q\eta$ given that the degree of entanglement is in the range $0 \le q \le 1$. This ellipsoid reduces to a point, $p_H = p_D = p_C = 0$, when $\sigma_{1P} = \sigma_{2P}$. Additionally, the ellipsoid is largest, for a fixed q, when one of the singular values is zero and $\eta = 1$. For the moment, we concentrate on a scheme with a source of photon pairs that have maximal entanglement $q = 1$, where the ellipsoid is a sphere with radius η.

We now use the formulated properties of the photon states to understand the need of the transformation M_P in the probe arm for object identification, noting that Eq. (5) gives a strict mathematical yet intuitive geometric understanding of the nonlocal discrimination problem using the Poincaré sphere. To this end, we illustrate the model with a set of three objects: a transparent object (quarter-wave plate) $\Omega_a = |H\rangle\langle H| + \exp(i\pi/2)|V\rangle\langle V|$ with singular values $\sigma_{1\Omega} = \sigma_{2\Omega} = 1$, a partially transparent object $\Omega_b = |H\rangle\langle H| + \exp[i(\pi/2 + 0.7i)]|V\rangle\langle V|$ with $\sigma_{1\Omega} = 1$ and $\sigma_{2\Omega} = 0.5$, and a fully polarizing object (horizontal polarizer) $\Omega_c = |H\rangle\langle H|$ with $\sigma_{1\Omega} = 1$ and $\sigma_{2\Omega} = 0$. These definitions are for an object rotation angle $\theta = 0$. Since rotation is a unitary transformation, the mentioned singular values of each object remain unaffected and the associated reference-photon reduced states lie on a sphere with a radius defined by Eq. (5) for all object angles. Since the considered objects have a rotation symmetry of π, we aim to have different ρ_R in the interval $0 \le \theta < \pi$ for the angle identification.

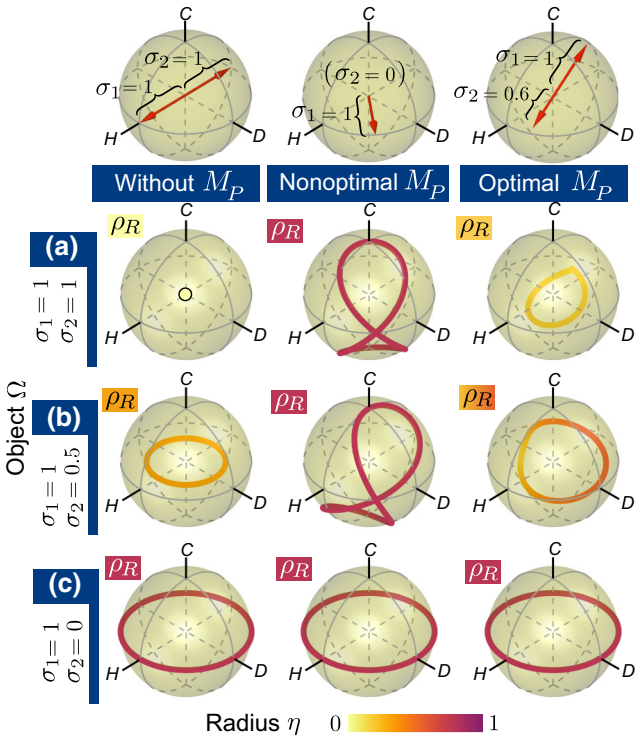

FIG. 2. Metasurface transformation M_P enabling the object discrimination. Top: the singular eigenvectors of M_P, scaled by the corresponding singular values, represented in the Poincaré sphere for the cases of (left) no metasurface, (middle) fully polarizing transformation, and (right) optimal partially polarizing. The axes of the Poincaré sphere correspond to horizontal (H), diagonal (D), and right circular (C) polarizations. (a)–(c) Reduced states of the reference photon after measuring the probe photon ρ_R produced by a set of three objects $\Omega_{a,b,c}$ for different M_P in each column. The curves are formed from the points corresponding to different object rotation angles in the range $0 \le \theta < \pi$.

We illustrate the effect of metasurface transformation M_P on the discrimination of objects in Fig. 2. We compare the cases of no metasurface with $M_P = I$ in the left, nonoptimal transformation in the middle, and optimized transformation in the right column. In the top row, we show in the Poincaré sphere the two orthonormal right singular vectors of M_P, $\mathbf{m}_{jP}$ with $j \in \{1, 2\}$ (see Appendix A), whose magnitude has been scaled with their corresponding singular value σ_{jP}. Rows (a)–(c) represent the normalized reduced states of the probe photon for the three chosen objects $\Omega_{a,b,c}$, respectively.

For the simplest scenario without a metasurface M_P in the probe arm presented in Fig. 2(left column), a fully transparent wave plate Ω_a always corresponds to a single point, such that its orientation angle cannot be identified. Indeed, in this case $T_P = \Omega$ with singular values $\sigma_P = \sigma_\Omega$, and according to Eq. (5) any transparent phase object with $\sigma_{1\Omega} = \sigma_{2\Omega}$ will generate reduced states ρ_R

that stay at the origin of the Poincaré sphere independent of the object's phase. Hence, nonlocal discrimination between transparent phase objects and determination of their rotations cannot be performed without a metasurface M_P acting on the polarization of the probe photon before a polarization-insensitive detector.

In Fig. 2(middle column), we illustrate a case of fully polarizing transformation M_P with $\sigma_{2P} = 0$, such that only one polarization is transmitted. This represents a quantum projection measurement for the state $\mathbf{m}_{1P}$. We note that if an object Ω and/or M_P have one singular value equal to zero then its product, $T_P = M_P\Omega$, also has one null singular value. This causes, according to Eq. (5), the reduced state of the reference photon to lie on the surface of the Poincaré sphere. Consequently, not all objects and rotation angles can be distinguished since the closed loops formed by the objects' reduced states would cross.

To enable discrimination in the general case, the ratio of the smaller to larger singular values of M_P has to be in the range $0 < \sigma_2/\sigma_1 < 1$, i.e., it should be a partially polarizing transformation. Additionally, its largest singular value should be close to 1 to ensure high photon counts. The reduced states for a numerically optimized polarization basis of M_P are shown in Fig. 2(right column). They do not cross and enable discrimination, confirming the above analysis of the required singular values. The displayed elliptical polarization basis is formed by the two orthonormal right singular vectors of M_P, represented by arrows in the top-row plot. Importantly, the optimal M_P depends on the given set of objects.

B. Operation and design of reference-arm metasurface

Next, we discuss conditions on the optimal polarization bases of the transformation M_R in the reference arm, which ensures that each object Ω has a unique pattern in the coincidences. To achieve practically relevant solutions, we impose two additional conditions: object identification must be achieved using a small number of outputs and the total number of photon counts in all outputs should be larger than zero for any object.

We note that a specially designed metasurface with four diffraction outputs can facilitate a full characterization of single-photon polarization [7], thereby allowing for object discrimination based on the different reference photon states ρ_R.

We find that discrimination between particular sets of objects may be performed with a smaller set of outputs, which can simplify the measurements and improve the signal-to-noise ratio since photon counts are concentrated in fewer outputs. The optimal design that meets these requirements can be investigated by writing the expectation value of the coincidence counts with the nth reference output as (see Appendix A)

$$\Gamma_n = \tfrac{1}{2}(\sigma_{1R,n}^2 + \sigma_{2R,n}^2) + \tfrac{1}{2}(\mathbf{p}\cdot\mathbf{m}_{1R,n})(\sigma_{1R,n}^2 - \sigma_{2R,n}^2), \tag{6}$$

where $\sigma_{R,n}$ stands for a singular value of the transformation $M_{R,n}$, and $\mathbf{m}_{R,n}$ is its right singular vector represented in the Poincaré sphere. Additionally, the output pattern in coincidences can be represented in a space $\mathcal{D}$ such that each expectation value Γ_n corresponds to a coordinate along the nth dimension and each pattern in coincidences is mapped as a point in $\mathcal{D}$.

One approach to fulfill the requirement of nonzero photon counts consists of having equal singular values for all outputs of the metasurface M_R, $\sigma_{1R,n} = \sigma_{1R}$ and $\sigma_{2R,n} = \sigma_{2R}$, and also that the sum of their right singular vectors be equal to zero, $\sum \mathbf{m}_{1R,n} = 0$. Thus, $\sum \Gamma_n = (1/2)\sum(\sigma_{1R}^2 + \sigma_{2R}^2)$ is a constant different from zero, meaning that the photon counts will be nonzero. If we consider M_R with three outputs, the condition $\sum \mathbf{m}_{1R,n} = 0$ would indicate that each pair of vectors $\mathbf{m}$ encloses an angle of 120° and they would all lie in one plane in the Poincaré sphere. This plane has to be chosen such that each object Ω has a unique pattern in the coincidences. To demonstrate this, we return to our example with objects $\Omega_{a,b,c}$.

The reduced states ρ_R from the objects $\Omega(\theta)$ and the optimal M_P discussed in Fig. 2 are depicted together in the Poincaré sphere of Fig. 3(a). A plane that can encompass the three vectors $\mathbf{m}$ while allowing for separation of the projected reduced states is illustrated in blue along with its normal $\mathbf{N}$. The projections of all the reduced states ρ_R into this plane are well separated, as shown in Fig. 3(b). They can then be mapped into the space $\mathcal{D}$ of the coincidences at the outputs using the three projection vectors of M_R depicted in Fig. 3(c), as described above. The direction of the optimal vector $\mathbf{N}$, and therefore the plane where the vectors $\mathbf{m}_{1R,n}$ lie can be found numerically. For the set of objects investigated here, at least three outputs are needed to achieve discrimination.

The optimal forms of M_P and M_R in each arm of the setup can be found numerically. We note that the polarization transformations in principle can also be implemented with a collection of bulk optical elements; however, at the expense of complex designs sensitive to alignment. Here we show that these polarization manipulations can be realized using nanostructured dielectric metasurfaces, which can effectively act as partial polarizers in arbitrary elliptical bases with any required extinction ratio [7,40]. Each metasurface is a flat optical element composed of a periodically repeated array of nanoresonators called metagratings, which in turn is formed by nanoresonators whose phase retardances and orientations are optimized. We perform optimization of the phase retardances and orientations

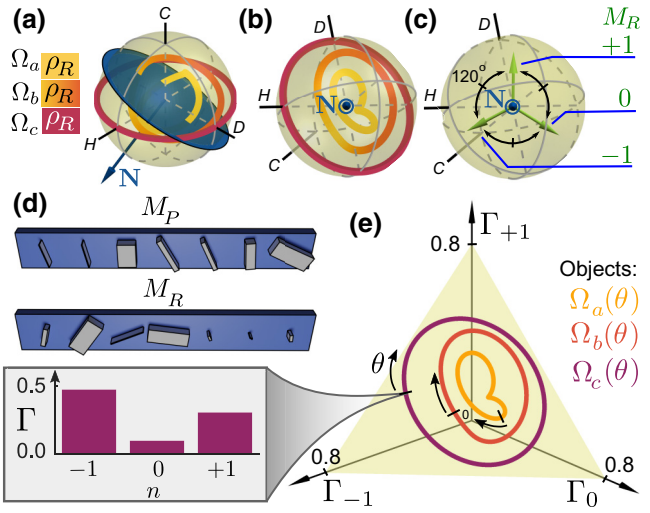

FIG. 3. (a),(b) Reduced state of the reference photon ρ_R produced by a set of three objects $\Omega_{a,b,c}$ and an optimal metasurface M_P corresponding to Fig. 2(right column) from two different perspectives. The vector **N** is normal to the blue plane where the optimal projection bases of the diffraction orders of the metasurface M_R are located; see (c). (d) Optimal metagratings in the probe M_P and reference M_R arms. (e) Coincidences at three diffraction orders Γ_{-1}, Γ_0, Γ_{+1}, showing that the objects can be discerned from one another and their own rotation angle θ unambiguously identified ($\theta = 0$ is marked with ticks, the object rotation symmetry is π). The inset shows one of the coincidence patterns.

associated with the individual nanoresonators to realize the required transformations.

Each dielectric nanoresonator located at position x of a metasurface can be represented using the Jones formalism as a rotated phase retarder

$$T(\theta,\phi_1,\phi_2;x) = \begin{bmatrix} \cos\theta & -\sin\theta \\ \sin\theta & \cos\theta \end{bmatrix} \begin{bmatrix} \exp(i\phi_1) & 0 \\ 0 & \exp(i\phi_2) \end{bmatrix} \times \begin{bmatrix} \cos\theta & \sin\theta \\ -\sin\theta & \cos\theta \end{bmatrix} \tag{7}$$

that results in a symmetric matrix, namely $T_{12} = T_{21}$. Similar to a conventional dielectric grating, the collective behavior of the nanoresonators will form diffraction orders in the far field. These are found by taking the Fourier series $\mathcal{F}$ of the ensemble $T(x)$ along x (note that, by calculating this series, the periodicity of the metagratings is automatically considered). Thus, each resulting diffraction order at position x' is defined by the symmetric transfer matrix

$$M(x') = \begin{bmatrix} \mathcal{F}(T_{11}) & \mathcal{F}(T_{12}) \\ \mathcal{F}(T_{21}) & \mathcal{F}(T_{22}) \end{bmatrix} \tag{8}$$

that depends on all the nanoresonators in the metagrating, each defined by its own parameters θ, ϕ_1, ϕ_2. The optimization algorithm finds the most adequate parameters for each nanoresonator so that each diffraction order M realizes a required polarization basis. Specifically, we design a metasurface for the probe arm such that its zeroth diffraction order realizes M_P. Similarly, a second metasurface is placed in the reference arm where the three outputs of M_R correspond to three diffraction orders, as illustrated in Fig. 1. The unit-cell geometries of numerically found optimal metagratings for the considered set of objects $\Omega_{a,b,c}$ are depicted in Fig. 3(d).

The main result of this work is shown in Fig. 3(e), where coincidence patterns at three diffraction orders for the objects $\Omega_{a,b,c}(\theta)$ are represented in the space $\mathcal{D} = \{\Gamma_{-1}, \Gamma_0, \Gamma_{+1}\}$, where each point on the plotted curves corresponds to a different object rotation angle θ. The inset shows an example for the polarizing object Ω_c at $\theta = 0$. This showcases that the full identification of objects with their corresponding rotation angle is possible by optimizing M_P and M_R. As designed, the chosen three outputs of metasurface M_R map the geometric shape of Fig. 3(b) into the space $\mathcal{D}$ in such a way that all the coincidences correspond to practically relevant nonzero photon counts.

III. ROLE OF THE DEGREE OF ENTANGLEMENT

After demonstrating that objects and their rotation angles can be discriminated using entangled states of light, next we show that the degree of entanglement is relevant when distinguishing specific classes of objects. To this end, we explore the effect of reducing the entanglement until reaching only classical correlation, $q = 0$. We consider a different set of polarization-sensitive objects that contains only generalized retarders $\Omega = |H\rangle\langle H| + \exp(i\phi)|V\rangle\langle V|$, each with its own phase difference ϕ between the horizontal and vertical polarization. Here, we do not seek to identify the rotation of each of them but just discern them based on ϕ.

The optimal M_P necessary to discern these phase objects for any value of q is a diagonal polarizer. Note here that this element can obviously be implemented simply using a conventional polarizer instead of a metasurface. The corresponding reduced states ρ_R of this set of phase objects are depicted in Fig. 4(a) for different levels of entanglement q. As can be seen, this chosen set of phase objects is a quite peculiar one because their reduced states have the same p_H Poincaré vector component [see Eq. (2)], as p_H does not depend on the phase ϕ. Furthermore, Eqs. (3) and (4) show that the lower the degree of entanglement, the smaller p_D and p_C become, as illustrated in Fig. 4(a) with a shrinking ellipsoid according to Eq. (5). In the case of only classical correlation between photons with $q = 0$, we have $p_D = p_C = 0$, such that all reduced states are in the same position and the different objects cannot be discriminated. It is worth noting that if phase objects of the type $\Omega = |H\rangle\langle H| + \exp(i\phi)|V\rangle\langle V|$ are rotated by an angle θ and an optimal M_P in the probe arm is

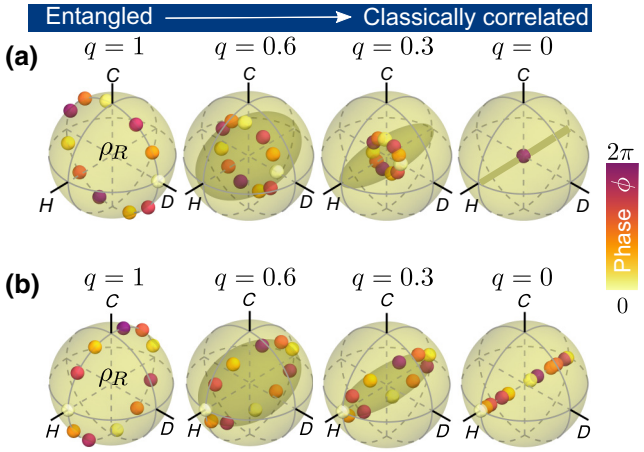

FIG. 4. Reduced state of the reference photon after measuring the probe photon ρ_R at different levels of entanglement. Here, the probe photon interacts with a set of different fully transmissive phase objects, $\Omega = |H\rangle\langle H| + \exp(i\phi)|V\rangle\langle V|$ (phase ϕ shown in the color scale), one at a time. (a) Not rotated $\theta = 0$ with optimal M_P that acts as a diagonal polarizer. (b) Rotated $\theta = 45^\circ$ with corresponding optimal M_P that is a horizontal polarizer.

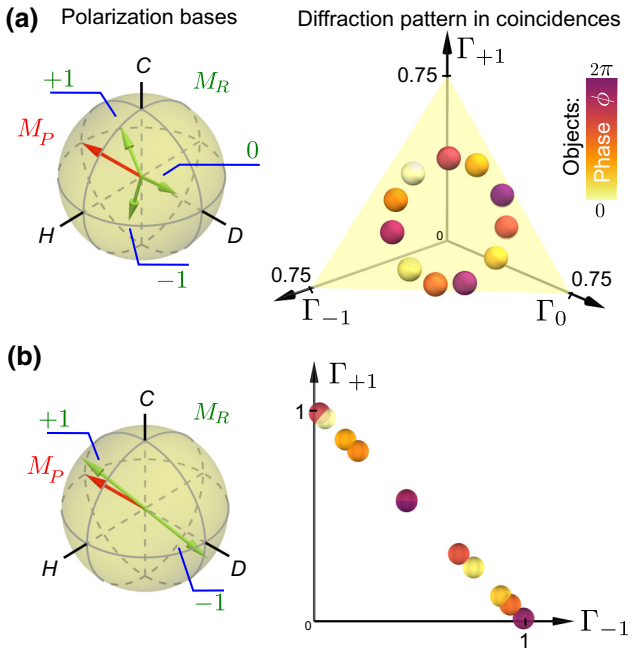

FIG. 5. Polarization bases of a metasurface M_R with (a) three and (b) two outputs along with the resulting diffraction patterns in coincidences. The set consists of phase objects and a diagonal polarizer M_P used in Fig. 4(a).

chosen, then the p_H component of the product $T_P = M_P\Omega$ can depend on the phase ϕ [this can be easily derived from Eqs. (2)–(4)]. Therefore, such phase objects can be told apart if a source with photon pairs that are classically correlated, $q = 0$, is used. Figure 4(b) illustrates an example with phase objects that are rotated 45° along with a horizontal polarizer as M_P, an optimal metasurface transformation found following the first stage of the design described in this manuscript. In contrast to Fig. 4(b), Fig. 4(a) illustrates that if the phase objects are not rotated then they cannot be identified. Moreover, note that the components $p_D = p_C = 0$ when $q = 0$; thus, the simplest element that can be used as M_R in the reference arm is a conventional polarizing beam splitter, which has two outputs, horizontal and vertical polarization.

In a nutshell, transformations T_P that have the same p_H component can only be discriminated if the photon-pair source has a high level of entanglement. Our conclusion on the advantage of entanglement generally agrees with the results of Ref. [9], where images of polarization-dependent patterns imprinted with a metasurface had higher visibility across different orientation angles for larger Bell parameter values.

Continuing with the discrimination protocol, it is known that a specially designed metasurface with four diffraction outputs can facilitate a full characterization of single-photon polarization [7], thereby allowing for object discrimination based on the different reference photon states ρ_R. Yet, discrimination between particular sets of objects may be performed with a smaller set of outputs. For the set of three objects of Fig. 3, three outputs were necessary. On the other hand, we show that two outputs of M_R can also identify objects and we demonstrate it by using the example of phase objects of Fig. 4(a). Figure 5 illustrates the resulting diffraction patterns in coincidences by using two different metasurfaces M_R that produce three and two diffraction orders, respectively. Each metasurface is optimized separately using the criteria explained in the second stage of the design. Although in both cases each object has a fingerprint, constraints of the photon measurements can define the minimum number of outputs required, e.g., the presence of noise in the measurements hindering the identification is an indicator that more outputs are needed.

IV. DISCUSSION AND SUMMARY

In summary, we have proposed a general approach for ghost discrimination between polarization-sensitive objects and simultaneous identification of their rotation through nonlocal measurements using nonclassical light. This is achieved by using ultrathin nanostructured metasurfaces designed to perform tailored polarization transformations with high robustness suitable for end-user applications, in contrast to traditional setups with multiple bulk optical elements requiring precise alignment. Moreover, we have showed that a full characterization of the reference photon with four correlation measurements might not be required for some sets of objects, where discrimination can be achieved with fewer coincidence measurements. We believe that these results can stimulate the practical development of efficient and integrated optical schemes

for characterization of objects with polarization-sensitive transmission characteristics across a broad spectral range. In particular, these can benefit applications demanding accurate discrimination of objects with various polarization characteristics, including biological samples with distinct birefringent and chiral features [41–43].

Additionally, we have shown that optimized metasurfaces can enable discrimination of multiple objects. Thereby, our approach paves the way to further research that focuses not only on the ultimate limit of the number of objects that can be discriminated, but also the possibility of facilitating the characterization of objects with spatially dependent polarization by, for example, exploiting the momentum correlation of each photon pair.

Furthermore, there is a potential to dynamically adapt the ghost polarimetry scheme for different target objects by employing tunable metasurfaces on the probe arm [44], whereas a static design of reference metasurface with four outputs is generic and suited for the discrimination of any polarization objects.

An entangled two-photon source considered above can facilitate precise ghost polarimetry at very low photon fluxes, which can be beneficial for measurements, especially with light-sensitive samples. On the other hand, when the use of bright illumination is appropriate, we found that a thermal source can also allow for polarization object discrimination, in analogy to other ghost imaging schemes [13,45–47]. We provide a detailed discussion in Appendix B, where we prove the similarity of correlations for entangled photon-pair and thermal sources and also identify their differences.

Lastly, a collection of the parameters of each optimized nanoresonator in each example can be found in Appendix C.

ACKNOWLEDGMENTS

The authors thank Michael Brodsky, Kai Wang, Shaun Lung, Jihua Zhang for insightful discussions and comments. This work is supported by the Thuringian Ministry for Economy, Science, and Digital Society (2021 FGI 0043), the German Federal Ministry of Education and Research (FKZ 13N14877), the German Research Foundation (IRTG 2675), the European Union through the ERASMUS+ program, the German Academic Exchange Service (Grant No. 57388353), and a UA-DAAD exchange scheme. A.A.S. also acknowledges support from the Australian Research Council (DP160100619, DP190101559, CE200100010) and US AOARD (19IOA053).

APPENDIX A: EXPECTATION VALUE OF THE *n*TH OUTPUT OF METASURFACE TRANSFORMATION M_R

The singular value decomposition of a transformation M is $M = U\Sigma V^\dagger$, where the columns of U (V) are the left (right) singular vectors and Σ is a diagonal matrix that contains the singular values. Furthermore, the expectation value of a density matrix ρ after the transformation M can be found by

$$I = \mathrm{tr}(M\rho M^\dagger) = \mathrm{tr}[(\Sigma V^\dagger)\rho(V\Sigma)], \tag{A1}$$

where we have used the cyclic property of the trace $\mathrm{tr}(ABC) = \mathrm{tr}(BCA)$ and the fact that U is unitary, $U^\dagger U = 1$. This shows that the expectation value Γ does not depend on the left singular vectors of M. Additionally, the density matrix of a two-level system can be represented in the Bloch sphere

$$\rho = \tfrac{1}{2}(1 + a_x X + a_y Y + a_z Z), \tag{A2}$$

where $a_{x,y,z}$ are the components of the Bloch vector $\mathbf{a}$, and X, Y, Z are the Pauli matrices. Therefore, the expectation value Γ is found to be

$$\begin{aligned} I &= \frac{\sigma_1^2}{2}(1 + \mathbf{a}\cdot\mathbf{A}_1) + \frac{\sigma_2^2}{2}(1 + \mathbf{a}\cdot\mathbf{A}_2) \\ &= \tfrac{1}{2}(\sigma_1^2 + \sigma_2^2) + \tfrac{1}{2}(\mathbf{a}\cdot\mathbf{A}_1)(\sigma_1^2 - \sigma_2^2), \end{aligned} \tag{A3}$$

where $\mathbf{A} = [A_x, A_y, A_z]$ is the representation of a right singular vector in the Bloch sphere. To arrive to the final expression, we used the fact that the singular vectors form an orthonormal basis, i.e., $\mathbf{A}_2 = -\mathbf{A}_1$. The x component of the first right singular vector is

$$A_{x1} = \mathrm{tr}\left[\left(\begin{bmatrix}1 & 0\\ 0 & 0\end{bmatrix} V^\dagger\right) X \left(V\begin{bmatrix}1 & 0\\ 0 & 0\end{bmatrix}\right)\right], \tag{A4}$$

a similar calculation is done to find the rest of the components. Lastly, since we are working with the state of the polarization of light, we translate the representation of the Bloch sphere to the Poincaré sphere with $\mathbf{p} = [a_z, a_x, -a_y]$ and $\mathbf{m} = [A_z, A_x, -A_y]$. This derivation leads to Eq. (6). Note there that, since $\mathbf{p}$ is derived from the reduced density matrix of the reference, i.e., carries the information of the measurement of the probe photon, the expectation value I becomes the expectation value of the two-photon coincidence counts Γ.

APPENDIX B: QUANTUM-ENTANGLED VERSUS THERMAL SOURCE

Consider a maximally entangled two-photon state, Eq. (1) for $q = 1$. Then, its wave function can be represented without loss of generality as

$$|\psi\rangle = \frac{1}{\sqrt{2}}(|\mathbf{v}_{1P}\mathbf{v}_{1P}\rangle + |\mathbf{v}_{2P}\mathbf{v}_{2P}\rangle), \tag{B1}$$

where $\mathbf{v}$ is a right singular, complex-valued vector of a Jones matrix V (of size 2×2). Note that $\mathbf{v}_{1P}$ and $\mathbf{v}_{2P}$ are

TABLE I. Parameters of the nanoresonators: the orientation angle θ and the phase delays for polarizations along the two axes $\phi_{1,2}$.

	Figure 3						Figure 5(a)			Figure 5(b)		
	M_P			M_R			M_R			M_R		
Nanoresonator	θ (deg)	ϕ_1	ϕ_2	θ (deg)	ϕ_1	ϕ_2	θ (deg)	ϕ_1	ϕ_2	θ (deg)	ϕ_1	ϕ_2
1	104.22	1.73	0.06	−15.66	0.42	−1.91	87.36	1.59	3.84	7.37	2.96	2.21
2	100.75	1.71	−0.06	53.68	3.56	1.67	−76.03	0.95	4.50	−31.41	3.49	1.69
3	0.45	−1.18	1.66	22.60	3.45	−0.10	136.21	0.07	−0.60	138.29	−1.94	0.90
4	28.39	0.33	2.48	−7.55	3.95	1.35	−16.02	0.17	−1.24	−148.62	−0.34	−1.32
5	24.42	−0.28	2.23	24.24	0.21	0.53	7.30	1.09	−1.39	−10.53	0.02	5.14
6	5.05	−0.62	1.91	−31.76	−0.27	0.09	25.92	1.65	−2.56	−126.71	−1.95	−5.46
7	62.79	1.07	2.69	3.33	0.29	−0.68	237.32	0.13	3.43	36.09	3.44	1.78

orthogonal unitary vectors. Then, the two-photon correlations can be found as

$$\Gamma_n^{(\text{two photon})} = \frac{1}{2}\sum_{q_P,q_R=1}^{2} |\mathbf{v}_{q_P P}\cdot\mathbf{v}_{q_R R,n}|^2 \sigma_{q_P P}^2 \sigma_{q_R R,n}^2, \quad \text{(B2)}$$

where σ are the singular values of the Jones matrices characterizing the transformation from the source to the detector in the probe (subscript P) and reference (subscript R,n) arms, and we choose an order $\sigma_1 \geq \sigma_2$. We note that $|\mathbf{v}_{1P}\cdot\mathbf{v}_{2R,n}|^2 + |\mathbf{v}_{2P}\cdot\mathbf{v}_{2R,n}|^2 = 1$, $|\mathbf{v}_{1P}\cdot\mathbf{v}_{1R,n}|^2 + |\mathbf{v}_{2P}\cdot\mathbf{v}_{1R,n}|^2 = 1$, $|\mathbf{v}_{1P}\cdot\mathbf{v}_{1R,n}|^2 + |\mathbf{v}_{1P}\cdot\mathbf{v}_{2R,n}|^2 = 1$. Then, we obtain

$$\begin{aligned}\Gamma_n^{(\text{two photon})} &= \tfrac{1}{4}(\sigma_{1P}^2+\sigma_{2P}^2)(\sigma_{1R,n}^2+\sigma_{2R,n}^2)\\ &\quad+\tfrac{1}{2}(\sigma_{1P}^2-\sigma_{2P}^2)(\sigma_{1R,n}^2-\sigma_{2R,n}^2)\\ &\quad\times(|\mathbf{v}_{1P}\cdot\mathbf{v}_{1R,n}|^2-1/2).\end{aligned} \quad \text{(B3)}$$

For comparison, we now consider a thermal source that has a classical polarization state $|\Psi_{\text{in}}\rangle$ that randomly changes in time. After interacting with a 50:50 beam splitter, the same source's polarization state can be found in the probe and in the reference arm at any fixed time. Then, the total intensity after optical element(s) with a Jones matrix V is

$$I = \sigma_1^2|\mathbf{v}_1\cdot\Psi_{\text{in}}|^2 + \sigma_2^2|\mathbf{v}_2\cdot\Psi_{\text{in}}|^2. \quad \text{(B4)}$$

Additionally, due to the orthogonality $\mathbf{v}_1\cdot\mathbf{v}_2 = 0$, $|\mathbf{v}_2\cdot\Psi_{\text{in}}|^2 + |\mathbf{v}_1\cdot\Psi_{\text{in}}|^2 = 1$, and, therefore,

$$I = (\sigma_1^2-\sigma_2^2)|\mathbf{v}_1\cdot\Psi_{\text{in}}|^2 + \sigma_2^2. \quad \text{(B5)}$$

We can then calculate the product of intensities of the probe and reference arm,

$$\begin{aligned}I_P I_{R,n} &= [(\sigma_{1P}^2-\sigma_{2P}^2)|\mathbf{v}_{1P}\cdot\Psi_{\text{in}}|^2+\sigma_{2P}^2]\\ &\quad\times[(\sigma_{1R,n}^2-\sigma_{2R,n}^2)|\mathbf{v}_{1R,n}\cdot\Psi_{\text{in}}|^2+\sigma_{2R,n}^2],\end{aligned} \quad \text{(B6)}$$

and represent an input state, assuming that its norm is unity, as

$$\Psi_{\text{in}} = \cos(\theta/2)\mathbf{v}_{1P} + \sin(\theta/2)e^{i\varphi}\mathbf{v}_{2P}. \quad \text{(B7)}$$

Then, using the property $|\mathbf{v}_{1P}\cdot\mathbf{v}_{1R,n}|^2 + |\mathbf{v}_{2P}\cdot\mathbf{v}_{1R,n}|^2 = 1$, we have

$$\begin{aligned}I_P &= (\sigma_{1P}^2-\sigma_{2P}^2)\cos^2(\theta/2)+\sigma_{2P}^2,\\ I_{R,n} &= (\sigma_{1R,n}^2-\sigma_{2R,n}^2)\{|\mathbf{v}_{1R,n}\cdot\mathbf{v}_{1P}|^2\cos(\theta)+\sin^2(\theta/2)\\ &\quad+\sin(\theta)\text{Re}[e^{-i\varphi}(\mathbf{v}_{1R}\cdot\mathbf{v}_{1P})(\mathbf{v}_{1R}\cdot\mathbf{v}_{2P})^*]\}+\sigma_{2R,n}^2.\end{aligned} \quad \text{(B8)}$$

The state Ψ_{in} can be represented with the density matrix $\rho_{\text{in}} = |\Psi_{\text{in}}\rangle\langle\Psi_{\text{in}}|$ whose Bloch vector is $\mathbf{a} = [\sin\theta\cos\phi, \sin\theta\sin\phi, \cos\theta]$, where $0 \leq \theta \leq \pi$ and $0 \leq \phi < 2\pi$ just like in a spherical coordinate system. Therefore, the intensity correlation after averaging over these ranges of angles is

$$\begin{aligned}\langle I_P I_{R,n}\rangle &= \frac{1}{2\pi}\int_0^{2\pi} d\varphi \frac{1}{\pi}\int_0^{\pi} d\theta I_P I_{R,n}\\ &= \tfrac{1}{4}(\sigma_{1P}^2+\sigma_{2P}^2)(\sigma_{1R,n}^2+\sigma_{2R,n}^2)\\ &\quad+\tfrac{1}{4}(\sigma_{1P}^2-\sigma_{2P}^2)(\sigma_{1R,n}^2-\sigma_{2R,n}^2)\\ &\quad\times(|\mathbf{v}_{1P}\cdot\mathbf{v}_{1R,n}|^2-1/2).\end{aligned} \quad \text{(B9)}$$

It is worth noting that the first term constitutes the background signal that is given by the product of the independent intensity fluctuations of each arm, $\langle I_P\rangle = (\sigma_{1P}^2+\sigma_{2P}^2)/2$ and $\langle I_{R,n}\rangle = (\sigma_{1R,n}^2+\sigma_{2R,n}^2)/2$, whereas the second term shows the intensity correlation between the two arms.

It is clear that the correlations for a two-photon entangled source in Eq. (B3) and a thermal source in Eq. (B9) have the same form except for a factor of two difference in their corresponding second terms that represent correlations above a background. This means that the thermal source can be used to obtain the polarization information from the object similar to an entangled source. However,

from the difference of the coefficients, we conclude that the entangled case will show better contrast than the thermal source. Additionally, an entangled two-photon source can allow precise measurements with much smaller photon fluxes, which is an important capability for various applications [48].

APPENDIX C: PARAMETERS OF THE NANORESONATORS OF EACH EXAMPLE

Table I shows a summary of the numerically calculated parameters of the nanoresonators in each of the presented examples.

[1] N.-J. Jan, J. L. Grimm, H. Tran, K. L. Lathrop, G. Wollstein, R. A. Bilonick, H. Ishikawa, L. Kagemann, J. S. Schuman, and I. A. Sigal, Polarization microscopy for characterizing fiber orientation of ocular tissues, Biomed. Opt. Express **6**, 4705 (2015).

[2] A. Puthukkudy, J. V. Martins, L. A. Remer, X. G. Xu, O. Dubovik, P. Litvinov, B. McBride, S. Burton, and H. M. J. Barbosa, Retrieval of aerosol properties from airborne hyper-angular rainbow polarimeter (airharp) observations during acepol 2017, Atmos. Meas. Tech. **13**, 5207 (2020).

[3] M. Chekhova and P. Banzer, *Polarization of Light In Classical, Quantum, and Nonlinear Optics* (De Gruyter, Berlin, 2021).

[4] A. Martinez, Polarimetry enabled by nanophotonics, Science **362**, 750 (2018).

[5] N. A. Rubin, G. D'Aversa, P. Chevalier, Z. J. Shi, W. T. Chen, and F. Capasso, Matrix Fourier optics enables a compact full-stokes polarization camera, Science **365**, eaax1839 (2019).

[6] T. Stav, A. Faerman, E. Maguid, D. Oren, V. Kleiner, E. Hasman, and M. Segev, Quantum entanglement of the spin and orbital angular momentum of photons using metamaterials, Science **361**, 1101 (2018).

[7] K. Wang, J. G. Titchener, S. S. Kruk, L. Xu, H. P. Chung, M. Parry, I. I. Kravchenko, Y. H. Chen, A. S. Solntsev, Y. S. Kivshar, D. N. Neshev, and A. A. Sukhorukov, Quantum metasurface for multiphoton interference and state reconstruction, Science **361**, 1104 (2018).

[8] P. Georgi, M. Massaro, K. H. Luo, B. Sain, N. Montaut, H. Herrmann, T. Weiss, G. X. Li, C. Silberhorn, and T. Zentgraf, Metasurface interferometry toward quantum sensors, Light Sci. Appl. **8**, 70 (2019).

[9] C. Altuzarra, A. Lyons, G. H. Yuan, C. Simpson, T. Roger, J. S. Ben-Benjamin, and D. Faccio, Imaging of polarization-sensitive metasurfaces with quantum entanglement, Phys. Rev. A **99**, 020101 (2019).

[10] A. S. Solntsev, G. S. Agarwal, and Y. S. Kivshar, Metasurfaces for quantum photonics, Nat. Photon. **15**, 327 (2021).

[11] H. Kellock, T. Setala, A. T. Friberg, and T. Shirai, Polarimetry by classical ghost diffraction, J. Opt. **16**, 055702 (2014).

[12] T. B. Pittman, Y. H. Shih, D. V. Strekalov, and A. V. Sergienko, Optical imaging by means of 2-photon quantum entanglement, Phys. Rev. A **52**, R3429 (1995).

[13] A. Valencia, G. Scarcelli, M. D'Angelo, and Y. Shih, Two-Photon Imaging with Thermal Light, Phys. Rev. Lett. **94**, 063601 (2005).

[14] K. W. C. Chan, M. N. O'Sullivan, and R. W. Boyd, Two-color ghost imaging, Phys. Rev. A **79**, 033808 (2009).

[15] S. Karmakar and Y. H. Shih, Two-color ghost imaging with enhanced angular resolving power, Phys. Rev. A **81**, 033845 (2010).

[16] R. S. Aspden, N. R. Gemmell, P. A. Morris, D. S. Tasca, L. Mertens, M. G. Tanner, R. A. Kirkwood, A. Ruggeri, A. Tosi, R. W. Boyd, G. S. Buller, R. H. Hadfield, and M. J. Padgett, Photon-sparse microscopy: Visible light imaging using infrared illumination, Optica **2**, 1049 (2015).

[17] B. I. Erkmen and J. H. Shapiro, Ghost imaging: From quantum to classical to computational, Adv. Opt. Photon. **2**, 405 (2010).

[18] G. Brida, M. Genovese, and I. R. Berchera, Experimental realization of sub-shot-noise quantum imaging, Nat. Photon. **4**, 227 (2010).

[19] P. A. Morris, R. S. Aspden, J. E. C. Bell, R. W. Boyd, and M. J. Padgett, Imaging with a small number of photons, Nat. Commun. **6**, 5913 (2015).

[20] A. Hannonen, A. T. Friberg, and T. Setala, Classical spectral ghost ellipsometry, Opt. Lett. **41**, 4943 (2016).

[21] A. Hannonen, A. T. Friberg, and T. Setala, Classical ghost-imaging spectral ellipsometer, J. Opt. Soc. Am. A **34**, 1360 (2017).

[22] P. Janassek, S. Blumenstein, and W. Elsasser, Recovering a hidden polarization by ghost polarimetry, Opt. Lett. **43**, 883 (2018).

[23] D. F. Shi, J. M. Zhang, J. Huang, Y. J. Wang, K. Yuan, K. F. Cao, C. B. Xie, D. Liu, and W. Y. Zhu, Polarization-multiplexing ghost imaging, Opt. Lasers Eng. **102**, 100 (2018).

[24] A. S. Chirkin, P. P. Gostev, D. P. Agapov, and S. A. Magnitskiy, Ghost polarimetry: Ghost imaging of polarization-sensitive objects, Laser Phys. Lett. **15**, 115404 (2018).

[25] A. Hannonen, B. J. Hoenders, W. Elsasser, A. T. Friberg, and T. Setala, Ghost polarimetry using stokes correlations, J. Opt. Soc. Am. A **37**, 714 (2020).

[26] M. Rosskopf, T. Mohr, and W. Elsasser, Ghost Polarization Communication, Phys. Rev. Appl. **13**, 034062 (2020).

[27] S. Magnitskiy, D. Agapov, and A. Chirkin, Ghost polarimetry with unpolarized pseudo-thermal light, Opt. Lett. **45**, 3641 (2020).

[28] H. C. Liu, B. A. Yang, Q. H. Guo, J. H. Shi, C. Y. Guan, G. X. Zheng, H. Muhlenbernd, G. X. Li, T. Zentgraf, and S. Zhang, Single-pixel computational ghost imaging with helicity-dependent metasurface hologram, Sci. Adv. **3**, e1701477 (2017).

[29] M. Malik, H. Shin, M. O'Sullivan, P. Zerom, and R. W. Boyd, Quantum Ghost Image Identification with Correlated Photon Pairs, Phys. Rev. Lett. **104**, 163602 (2010).

[30] S. Slussarenko and G. J. Pryde, Photonic quantum information processing: A concise review, Appl. Phys. Rev. **6**, 041303 (2019).

[31] H. L. Huang, D. C. Wu, D. J. Fan, and X. B. Zhu, Superconducting quantum computing: A review, Sci. China-Inf. Sci. **63**, 180501 (2020).

[32] N. Gisin and R. Thew, Quantum communication, Nat. Photon. **1**, 165 (2007).
[33] V. Giovannetti, S. Lloyd, and L. Maccone, Advances in quantum metrology, Nat. Photon. **5**, 222 (2011).
[34] L. Pezze, A. Smerzi, M. K. Oberthaler, R. Schmied, and P. Treutlein, Quantum metrology with nonclassical states of atomic ensembles, Rev. Mod. Phys. **90**, 035005 (2018).
[35] W. K. Wootters, Entanglement of Formation of an Arbitrary State of two Qubits, Phys. Rev. Lett. **80**, 2245 (1998).
[36] A. Aspect, P. Grangier, and G. Roger, Experimental Realization of Einstein-Podolsky-Rosen-Bohm Gedankenexperiment - a new Violation of Bell Inequalities, Phys. Rev. Lett. **49**, 91 (1982).
[37] N. A. Peters, J. T. Barreiro, M. E. Goggin, T. C. Wei, and P. G. Kwiat, Remote State Preparation: Arbitrary Remote Control of Photon Polarization, Phys. Rev. Lett. **94**, 150502 (2005).
[38] A. Z. Goldberg, P. De La Hoz, G. Bjork, A. B. Klimov, M. Grassl, G. Leuchs, and L. L. Sanchez-Soro, Quantum concepts in optical polarization, Adv. Opt. Photon. **13**, 1 (2021).
[39] M. Born and E. Wolf, *Principles of Optics: Electromagnetic Theory of Propagation, Interference and Diffraction of Light* (Cambridge University Press, UK, 2020), 7th ed.
[40] S. Lung, K. Wang, K. Z. Kamali, J. H. Zhang, M. Rahmani, D. N. Neshev, and A. A. Sukhorukov, Complex-birefringent dielectric metasurfaces for arbitrary polarization-pair transformations, ACS Photonics **7**, 3015 (2020).
[41] J. F. deBoer, T. E. Milner, M. J. C. vanGemert, and J. S. Nelson, Two-dimensional birefringence imaging in biological tissue by polarization-sensitive optical coherence tomography, Opt. Lett. **22**, 934 (1997).
[42] V. V. Tuchin, L. V. Wang, and D. A. Zimnyakov, *Optical Polarization in Biomedical Applications* (Springer, Berlin, 2006).
[43] P. Scott, X. Garcia-Santiago, D. Beutel, C. Rockstuhl, M. Wegener, and I. Fernandez-Corbaton, On enhanced sensing of chiral molecules in optical cavities, April **7**, 041413 (2020).
[44] C. U. Hail, A. K. U. Michel, D. Poulikakos, and H. Eghlidi, Optical metasurfaces: Evolving from passive to adaptive, Adv. Opt. Mater. **7**, 1801786 (2019).
[45] J. H. Shapiro, D. Venkatraman, and F. N. C. Wong, Classical imaging with undetected photons, Sci. Rep. **5**, 10329 (2015).
[46] R. S. Bennink, S. J. Bentley, and R. W. Boyd, Two-Photon Coincidence Imaging with a Classical Source, Phys. Rev. Lett. **89**, 113601 (2002).
[47] A. Gatti, E. Brambilla, M. Bache, and L. A. Lugiato, Ghost Imaging with Thermal Light: Comparing Entanglement and Classical Correlation, Phys. Rev. Lett. **93**, 093602 (2004).
[48] P. A. Moreau, E. Toninelli, T. Gregory, and M. J. Padgett, Imaging with quantum states of light, Nat. Rev. Phys. **1**, 367 (2019).